Journal of
Materials Chemistry A

ROYAL SOCIETY
OF CHEMISTRY

PAPER

View Article Online
View Journal | View Issue

Cite this: *J. Mater. Chem. A*, 2024, **12**, 14517

Synergistically coupling CoS/FeS_2 heterojunction nanosheets on a MXene *via* a dual molten salt etching strategy for efficient oxygen evolution reaction†

Zuliang Zhang,‡[a] Tian Liang,‡[b] Chulong Jin,[a] Shuyi Zhang,[d] Yuanyuan Cui,*[c] Jinxing Chen *[d] and Xiaojun Zeng *[a]

Metal sulfides exhibit good catalytic activity for the oxygen evolution reaction (OER) due to their distinctive electronic and structural properties; however, their inadequate electrical conductivity hinders electron transfer, while easy agglomeration obstructs active sites. Herein, a dual molten salt etching strategy and subsequent sulfidation are employed to anchor CoS/FeS_2 heterojunction nanosheets onto an electrically conductive MXene (MXene@CoS/FeS_2) for efficient OER. The strong electronic interaction between CoS and FeS_2, in conjunction with the conductive MXene, facilitates rapid charge transfer, while the heterostructured nanosheets on the MXene substrate expose abundant catalytic active sites. Dut to its delicate nanostructure, the MXene@CoS/FeS_2 composite demonstrates an exceptionally low overpotential (278 mV achieved at 10 mA cm^{-2}) and remarkable stability (over 40 h). Density functional theory (DFT) calculations indicate that the electron transfer at the CoS/FeS_2 interface effectively reduces the energy barrier of the rate-determining step (RDS) for MXene@CoS/FeS_2. Additionally, the simple and straightforward preparation process eliminates the need for HF, enabling efficient and large-scale catalyst production while ensuring safety and environmental friendliness. Overall, the designed MXene@CoS/FeS_2 holds great promise as an OER catalyst.

Received 26th March 2024
Accepted 10th May 2024

DOI: 10.1039/d4ta01999g

rsc.li/materials-a

Jinxing Chen

Jinxing Chen is currently an Associate professor of Soochow University. Before this, he was a postdoctoral fellow at the University of California, Riverside (UCR) under the supervision of Prof. Yadong Yin. He obtained his PhD degree from the University of Science and Technology of China (USTC) in 2018. From 2016 to 2018, he carried out research under the supervision of Prof. Yadong Yin at the University of California, Riverside (UCR). His current research interests focus on photothermal conversion and catalysis of nanomaterials.

1. Introduction

The transition from fossil fuels to renewable hydrogen for powering the planet is crucial in achieving carbon neutrality.[1–3] The process of electrochemical water splitting provides an environmentally sustainable method for producing hydrogen. The oxygen evolution reaction (OER) is the rate-determining step in the water splitting process, as it involves a sluggish four-electron–proton coupling reaction, whereas the hydrogen evolution reaction (HER) is merely a two-electron transfer reaction.[4–6] Synthesizing efficient catalysts for the OER is therefore a crucial step in water splitting. Currently, noble metal-based materials (*e.g.*, Ir/Ru and their oxides) are extensively employed as catalysts for the OER, yet they are still limited by scarcity and high cost.[7–10] Consequently, the abundant and cost-effective transition metal sulfides (TMSs) have attracted

---

[a] *National Engineering Research Center for Domestic & Building Ceramics, School of Materials Science and Engineering, Jingdezhen Ceramic University, Jingdezhen 333403, China. E-mail: zengxiaojun@jcu.edu.cn*

[b] *Hubei Key Laboratory of Radiation Chemistry and Functional Materials, School of Nuclear Technology and Chemistry & Biology, Hubei University of Science and Technology, Xianning 437100, China*

[c] *School of Materials Science and Engineering, Shanghai University, Shanghai 200444, China. E-mail: cui-yy@shu.edu.cn*

[d] *Institute of Functional Nano & Soft Materials (FUNSOM), Joint International Research Laboratory of Carbon-Based Functional Materials and Devices, Jiangsu Key Laboratory for Carbon-Based Functional Materials & Devices, Soochow University, Suzhou 215123, China. E-mail: chenjinxing@suda.edu.cn*

† Electronic supplementary information (ESI) available. See DOI: https://doi.org/10.1039/d4ta01999g

‡ These authors contributed equally to this work.

much attention, and the OER performance can be improved through the regulation of their properties.[11] One approach to enhance the OER efficiency of TMSs involves manipulating their crystal structure and morphology, such as synthesizing nanospheres, nanowires, or nanosheets, in order to increase both the specific surface area and the number of active sites.[12–15] Another approach is constructing heterostructures, such as integrating TMSs with metal oxides or metal phosphides, to create unique interfaces and more active sites.[16] However, the inferior electrical conductivity of TMSs impedes electron transfer, while structural collapse and aggregation during water splitting obstruct active sites, thereby restricting TMSs from being among the top catalysts for the OER.[17,18]

Two-dimensional (2D) transition metal carbides/nitrides (MXenes) exhibit the properties of high electrical conductivity, large surface area, hydrophilicity, and long-term stability, rendering them suitable substrates for TMSs in the OER.[19–23] Various studies have aimed to combine TMSs with MXenes for efficient OER. For example, Han *et al.*[24] anchored CoS_2 nanowires on the electronegative surfaces of exfoliated MXene nanosheets *via* a hydrothermal reaction followed by sulfidation. The stronger electronegativity of the MXene than that of CoS_2 promotes electron transfer from CoS_2 to the MXene matrix, while CoS_2 nanowires prevent aggregation of MXene nanosheets and further boost the mass transfer of reactants, all contributing to the improved OER activity and long-term stability of the CoS_2@MXene. Xie *et al.*[25] developed an adsorption–growth route to construct a MXene@FeS_2 composite. The MXene can not only modify the electrophilicity of the active centers of FeS_2 by modulating the electron density but also prevent the FeS_2 from aggregating, thereby enhancing the activity and stability of MXene@FeS_2 in the OER. Zou *et al.*[26] proposed a metal organic framework-based approach to immobilize porous NiCoS onto exfoliated $Ti_3C_2T_x$ MXene sheets. The strong interaction between NiCoS and $Ti_3C_2T_x$ facilitates electron transport, while the hierarchical structure of the NiCoS/$Ti_3C_2T_x$ provides more active sites, both owing to its superior activity in the OER. The current progress has been significant, yet challenges still remain: the integration of TMSs and MXenes typically involves a laborious fabrication process and necessitates the utilization of hazardous HF. Therefore, it is highly desired to fabricate TMSs/MXene composites through a simple, safe, and eco-friendly approach.

In light of this, CoFe alloy nanoparticles were anchored onto an electrically conductive MXene *via* a dual molten salt etching strategy, and the subsequent sulfidation *in situ* transforms CoFe nanoparticles into CoS/FeS_2 heterostructure nanosheets, resulting in MXene@CoS/FeS_2 heterostructures. The above approach has several advantages: (1) the method avoids the use of HF, which ensures safety and environmental friendliness. (2) The method is simple and straightforward, which can realize the efficient production of the MXene@CoS/FeS_2. (3) The method is solvent-free, which mitigates the oxidation of the MXene. The obtained MXene@CoS/FeS_2 also demonstrates various advantages stemming from its intricate nanostructure: (1) the CoS/FeS_2 heterostructure nanosheets offer abundant interfacial active sites. (2) The unblocked channels within layered MXene boost electron transfer. (3) The strong electronic interaction between CoS and FeS_2, along with the interfacial electronic coupling between the MXene and CoS/FeS_2 *via* Ti–O–Co and Ti–O–Fe bonds, enhances the electron transfer kinetics and ensures structural stability. Consequently, the MXene@CoS/FeS_2 composite exhibits a remarkably low overpotential (278 mV achieved at 10 mA cm^{-2}) and outstanding stability (over 40 h). Density functional theory (DFT) calculations indicate that the electron transfer at the CoS/FeS_2 interface effectively reduces the energy barrier of the rate-determining step (RDS) for MXene@CoS/FeS_2. This work validates the molten salt etching route in preparing the "TMS heterostructures + MXene" composite, which may inspire more researchers to develop catalysts that integrate MXenes with multi-transition metal chalcogenides, phosphides, *etc.*, for efficient OER.

2. Experimental section

2.1. Materials

Ti_3AlC_2 MAX (≥99%, 200 mesh) was purchased from Laizhou Kai Xi Ceramic Materials Co., Ltd. Sodium chloride (NaCl, ≥99.8%), potassium chloride (KCl, ≥99.9%), ferrous chloride tetrahydrate ($FeCl_2 \cdot 4H_2O$, ≥99.0%), cobalt chloride hexahydrate ($CoCl_2 \cdot 6H_2O$, ≥99.0%), thiourea (CH_4N_2S, ≥99.0%), and potassium hydroxide (KOH, ≥95%) were purchased from China National Pharmaceutical Group Chemical Reagent Corporation and used directly without further purification.

2.2. Synthesis of MXene@$Co_{0.7}Fe_{0.3}$

Firstly, Ti_3AlC_2 MAX (0.2 g), $CoCl_2 \cdot 6H_2O$ (0.549 g), and $FeCl_2 \cdot 4H_2O$ (0.153 g) were mixed in an agate mortar and thoroughly ground for 10 min. Secondly, NaCl (0.14 g) and KCl (0.152 g) were added to the aforementioned mixture and ground for 20 min, ensuring thorough grinding and uniform mixing of raw materials during the grinding process. The resulting mixture was then loaded into an alumina crucible and transferred to a tube furnace, where it was annealed to 750 °C at a heating rate of 4 °C min^{-1} under an argon atmosphere and maintained for 8 h. The product was washed with deionized water to remove residual inorganic salts, and vacuum-dried at 70 °C to obtain MXene@$Co_{0.7}Fe_{0.3}$. The control samples of MAX@NaCl/KCl, MXene@Co, and MXene@Fe were prepared using the above method with a slight modification in the first step regarding the inclusion of inorganic salts, with the addition of nothing, only $CoCl_2 \cdot 6H_2O$, and only $FeCl_2 \cdot 4H_2O$, respectively.

2.3. Synthesis of MXene@CoS/FeS_2

The MXene@$Co_{0.7}Fe_{0.3}$ (10 mg) and thiourea (120 mg) were placed in two alumina crucibles inside a tube furnace, with the thiourea located upstream. The furnace was heated to 350 °C at 4 °C min^{-1} under an Ar atmosphere and held for 2 h to obtain the MXene@CoS/FeS_2. The control samples of MAX@NaCl/KCl–S, MXene@CoS, and MXene@FeS_2 were synthesized similar to the above sulfidation method. The pure CoS/FeS_2 was prepared without adding MAX.

To further investigate the OER performance of the samples, the optimization experiments for MXene@CoS/FeS_2 were carried out by changing the addition of MAX (0.1, 0.2, and 0.3 g), mole ratios of Co/Fe salts (0 : 1, 1 : 1, 2 : 1, 3 : 1, 4 : 1, 1 : 3, and 1 : 0), and sulfidation temperatures (300, 350, and 450 °C). The MXene was obtained by stirring MXene@$Co_{0.7}Fe_{0.3}$ in a 0.5 M H_2SO_4 solution for 24 h, followed by washing and drying.

Details of the characterization, electrocatalytic measurements, and DFT calculation are shown in the ESI.†

3. Results and discussion

The synthetic schematic of MXene@CoS/FeS_2 is illustrated in Fig. 1. Firstly, the Ti_3AlC_2 MAX is uniformly mixed with $CoCl_2\cdot 6H_2O$, $FeCl_2\cdot 4H_2O$, NaCl, and KCl, followed by annealing under Ar to synthesize the MXene@$Co_{0.7}Fe_{0.3}$ *via* a dual molten salt etching strategy. During this process, the Lewis acid molten salts of $CoCl_2\cdot 6H_2O$ and $FeCl_2\cdot 4H_2O$ oxidize the almost zero-valence Al to Al^{3+}, while the Co^{2+} and Fe^{2+} are reduced to metallic Co and Fe, respectively, with the Co and Fe atoms are anchored onto the $Ti_3C_2T_x$ MXene substrate through the Ti–O–Co and Ti–O–Fe interfacial bonds. Meanwhile, the Cl^- is coordinated with Al^{3+} to form $AlCl_3$, which undergoes sublimation at temperatures above 178 °C. Secondly, the MXene@$Co_{0.7}Fe_{0.3}$ is sulfurized, leading to the *in situ* conversion of $Co_{0.7}Fe_{0.3}$ nanoparticles into CoS/FeS_2 heterostructure nanosheets and the formation of MXene@CoS/FeS_2. The preparation process is simple and straightforward, enabling large-scale production of MXene@CoS/FeS_2. Additionally, the process eliminates the need for HF, which ensures both safety and environmental friendliness.

The morphology of the samples was revealed by scanning electron microscopy (SEM). Ti_3AlC_2 MAX exhibited a relatively smooth surface (Fig. 2a) and a block-like morphology with dense interlayers (Fig. S1†). After etching with NaCl and KCl, a small amount of sheet-like structures formed on MAX@NaCl/KCl (Fig. 2b and S2†), which may have resulted from the vertical growth of sodium or potassium-related crystals on the surface during the crystallization process. The layered structure is also observed, which is due to the expansion of the Ti–Al–Ti layers by the high-temperature molten salt. After sulfurization, the layered structure of MAX@NaCl/KCl–S became more pronounced, possibly due to the sulfurization process further aggravating the removal of the Al intermediate layer. This can be reflected in both the cross-section and the surface of MAX@NaCl/KCl–S (Fig. 2c, d, S3, and S4†). After the addition of cobalt salt and iron salt for the molten salt etching process, SEM images of the cross-section show the transformation of Ti_3AlC_2 MAX into MXene@$Co_{0.7}Fe_{0.3}$ with a larger interlayer spacing (Fig. 2e and S5†), indicating that the addition of cobalt salt and iron salt successfully etched the Al layers to form an accordion-like $Ti_3C_2T_x$ MXene. Furthermore, on the surface of MXene@$Co_{0.7}Fe_{0.3}$, ultrathin nanosheets are visible, distributed on the accordion-like $Ti_3C_2T_x$ MXene substrate (Fig. 2f and S6†). The energy-dispersive X-ray spectroscopy (EDS) elemental mapping images of the cross-section of MXene@$Co_{0.7}Fe_{0.3}$ (Fig. 2g and S7†) show a uniform distribution of Co and Fe elements on the MXene substrate. After sulfurization, the accordion-like structure of the MXene is clearly visible from the cross-section of MXene@CoS/FeS_2 (Fig. 2h and S8†). Numerous nanosheets formed *in situ* are densely anchored on the MXene substrate (Fig. 2i and S9†). From the energy-dispersive X-ray spectroscopy (EDS) elemental mapping images of the surface (Fig. 2j and S10†) and cross-section (Fig. S11†) of MXene@CoS/FeS_2, a uniform distribution of Co, Fe, and S elements on the MXene substrate can be observed. Combined with the XRD results below, it can be concluded that these nanosheets belong to CoS/FeS_2 species. These results further confirm that a larger number of CoS/FeS_2 nanosheets uniformly grow on the interlayer and surface of the MXene matrix.

We also investigated the morphology of other control samples. In the SEM image of MXene@CoS (Fig. S12†), the CoS is predominantly present in a granular morphology, accompanied by a minor presence of sheet-like structures observed on its

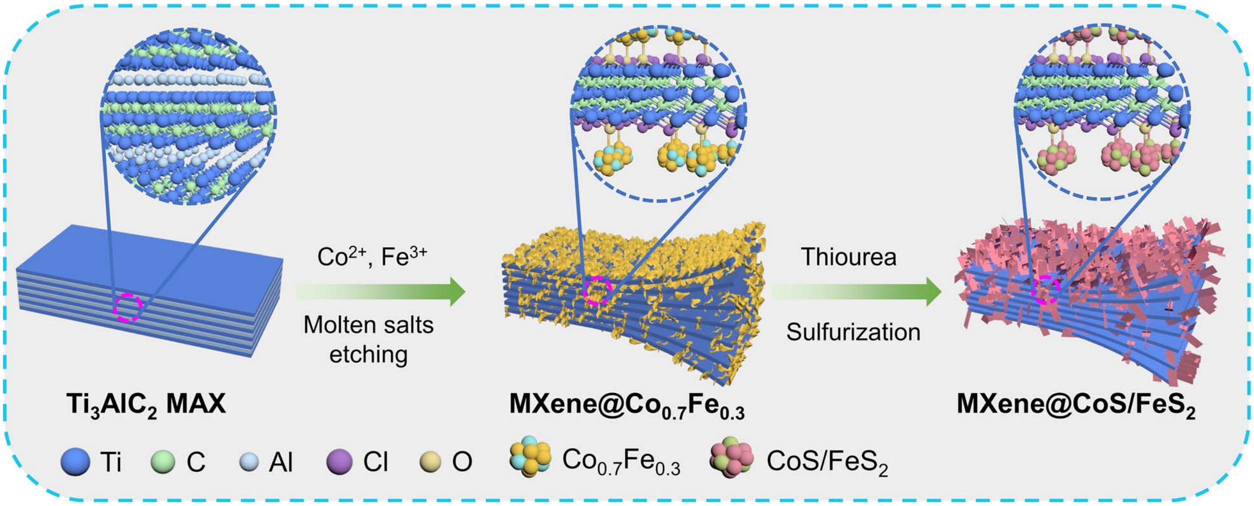

Fig. 1 Illustration for the synthesis of MXene@CoS/FeS_2.

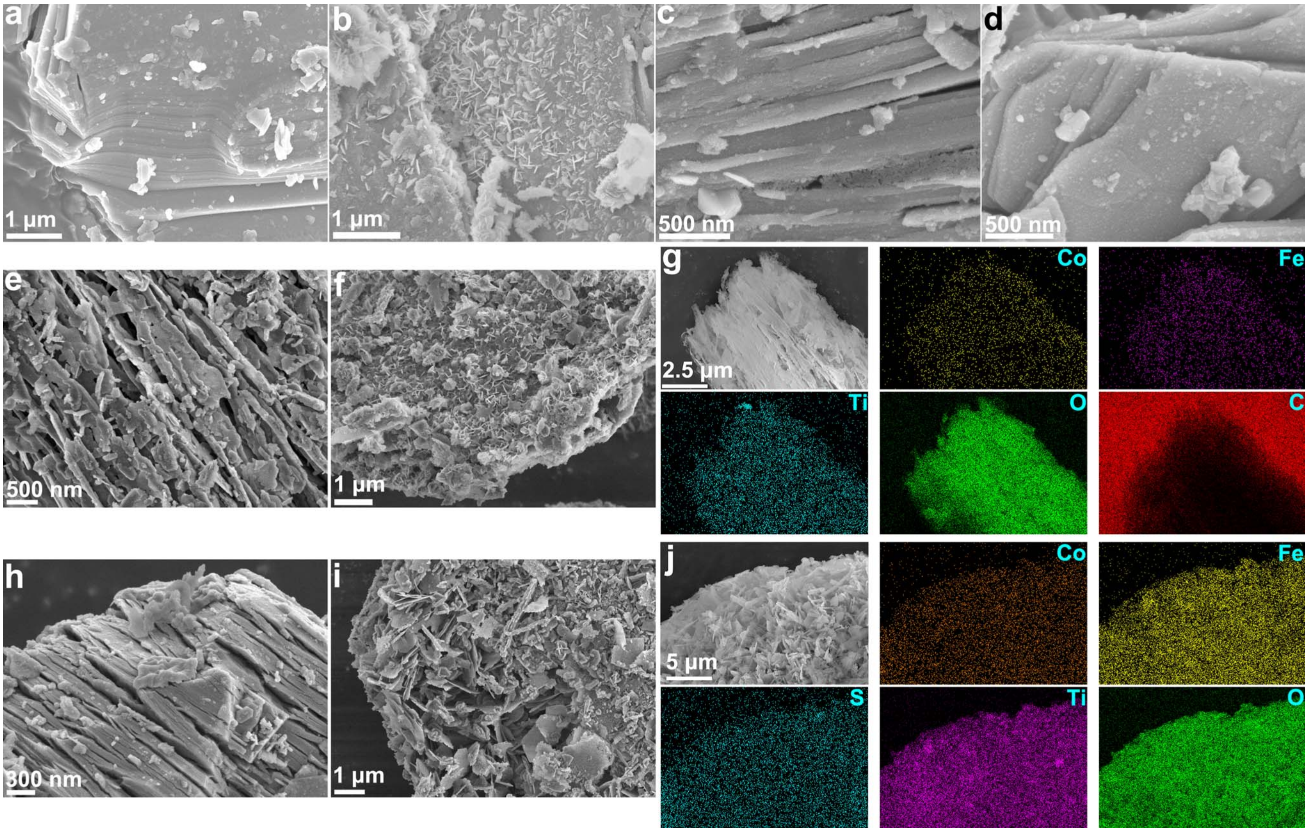

Fig. 2 SEM images of (a) Ti_3AlC_2 MAX, (b) MAXNaCl/KCl, (c, d) MAX@NaCl/KCl–S, (e, f) MXene@$Co_{0.7}Fe_{0.3}$, and (h, i) MXene@CoS/FeS_2. (g) EDS elemental mapping images of (g) MXene@$Co_{0.7}Fe_{0.3}$ and (j) MXene@CoS/FeS_2.

cross-section. These sheet-like structures bear a resemblance to the undissolved NaCl and KCl structures observed in MAX@NaCl/KCl. However, in its EDS image (Fig. S13†), a uniform distribution of Co and S elements can be seen on the cross-section and surface, indicating that these sheet-like structures are also composed of CoS. Similar results to MXene@CoS are observed in the SEM and EDS images of MXene@FeS_2 (Fig. S14 and S15†). Only a small amount of uneven FeS_2 nanosheets appeared in the MXene. Other studies have suggested that the introduction of iron promotes the formation of nanosheet structures in the CoFe alloy, further driving the formation of CoS/FeS_2 nanosheets.[27] The presence of numerous CoS/FeS_2 nanosheets contributes to the large specific surface area of MXene@CoS/FeS_2, thereby exposing plenty of catalytic active sites. Meanwhile, the abundant gaps between the nanosheets facilitate electrolyte storage and enhance mass transfer. The intricate nanostructure of MXene@CoS/FeS_2 will promote the electrocatalytic process and yield exceptional performance in the OER.

The transmission electron microscope (TEM) images reveal the microstructure of MAX@NaCl/KCl–S (Fig. 3a, b, and S16†). It can be seen that the synthesized MAX@NaCl/KCl–S exhibits ultrathin nanosheets, tending towards a monolayer and exhibiting a large number of pores. This indicates that the molten salt strategy at high temperature can effectively promote the formation of a MXene monolayer. At high resolution, lattice fringes corresponding to the (105) plane of MXene are observed (Fig. 3c and d), with a spacing of 0.216 nm.[28] This indicates successful removal of the Al layer. TEM images further reveal the microstructure of the surface and cross-section for MXene@CoS/FeS_2, as shown in Fig. 3e, f, S17, and S18.† A top-view of CoS/FeS_2 nanosheets on the surface of MXene can be observed, where CoS/FeS_2 nanosheets are precisely grown on the interlayer and surface of the MXene matrix. In the high-resolution TEM image (Fig. 3g), the red line area corresponds to the (100) plane of CoS with a lattice spacing of 0.293 nm, while the pink line area corresponds to the (111) plane of FeS_2 with a lattice spacing of 0.16 nm. Fig. S19† displays the high-resolution TEM images of the MXene substrate, showing lattice fringes of 0.32 nm, which can be assigned to the (104) plane of MXene.[29] The high-resolution TEM images of nanosheets at the edge of the MXene show a lattice fringe of 0.253 nm (Fig. 3h), corresponding to the (101) plane of CoS. Fig. 3i and j illustrate the low-magnification top-view of CoS/FeS_2 nanosheets on the MXene matrix, revealing the tight integration between the MXene and CoS/FeS_2 heterostructure. In the high-resolution TEM image (Fig. 3k), lattice spacings of 0.293 nm and 0.266 nm are also observed, corresponding to the (100) plane of CoS and the (002) plane of FeS_2, respectively. The appearance of FeS_2 and CoS phases may be due to partial phase separation during the sulfurization process,[30] which is consistent with the XRD and XPS results below. Additionally, lattice

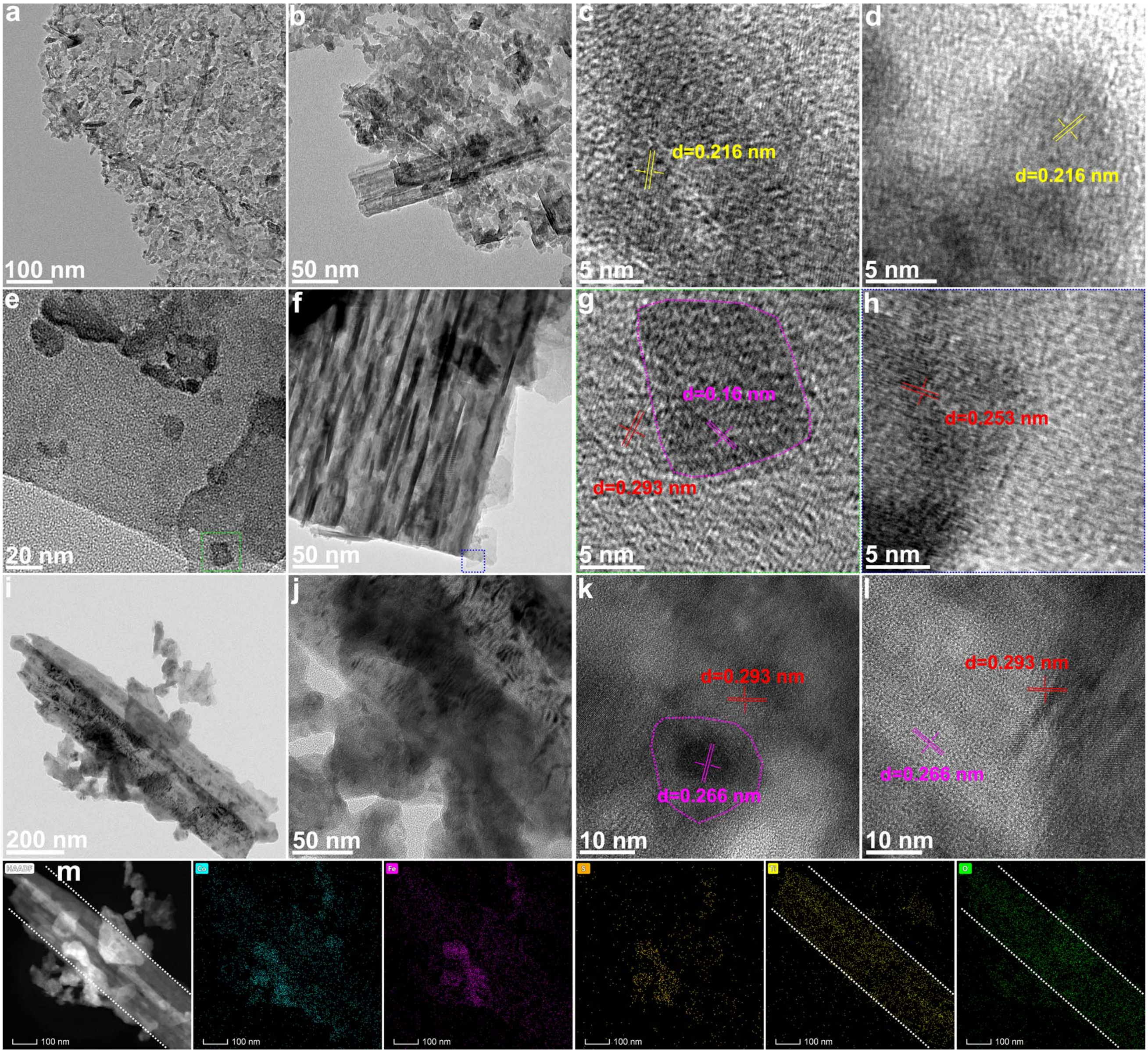

Fig. 3 (a, b, e, f, i, j) TEM and (c, d, g, h, k, l) HRTEM images of (a–d) MAX@NaCl/KCl–S and (e–l) MXene@CoS/FeS$_2$. (m) EDS elemental mapping images of MXene@CoS/FeS$_2$.

fringes of CoS and FeS$_2$ are further observed in the MXene substrate region (Fig. 3l). Both high-resolution TEM images in Fig. 3g–l show that CoS and FeS$_2$ grains are attached to each other at the nanoscale, forming a heterojunction. Numerous studies have demonstrated that close interface contacts in heterojunctions can effectively alleviate electron transfer resistance, shorten electron transfer distance, and provide more active sites for catalytic reactions.[31–35] In the EDS elemental mapping of MXene@CoS/FeS$_2$ (Fig. 3m), the dashed lines indicate the MXene substrate, and the uniform distribution of Co, Fe, and S elements on the nanosheets can be observed through the distribution areas of Ti and O. These results reveal the microstructure of MXene@CoS/FeS$_2$, where CoS/FeS$_2$ heterojunction nanosheets are densely anchored on the layered Ti$_3$C$_2$T$_x$ MXene.

An X-ray diffractometer (XRD) was adopted to collect crystallographic information on the samples. As shown in Fig. 4a, the Ti$_3$AlC$_2$ displays typical diffraction peaks at 33.9°, 39.1°, and 41.6°, corresponding to the (101), (104), and (105) crystal planes of the MAX phase (PDF#52-0875), respectively.[36,37] After the molten salt etching process, these peaks in MXene@Co$_{0.7}$Fe$_{0.3}$ significantly diminish or disappear, and the characteristic peak (002) at 9.54° shifts to a lower angle ($2\theta = 7.94°$), indicating the successful removal of Al from the Ti$_3$AlC$_2$ MAX. Meanwhile, the intensity of the (002) peak decreases significantly, which might be ascribed to changes in the stacking mode of atoms and axial periodic symmetry resulting from the substitution of Al with Co and Fe.[36,38] MXene@Co$_{0.7}$Fe$_{0.3}$ exhibits peaks at 45.06° and 65.63° that correspond to the (110) and (200) planes of the Co$_{0.7}$Fe$_{0.3}$ alloy (PDF#48-1818), respectively. This indicates the

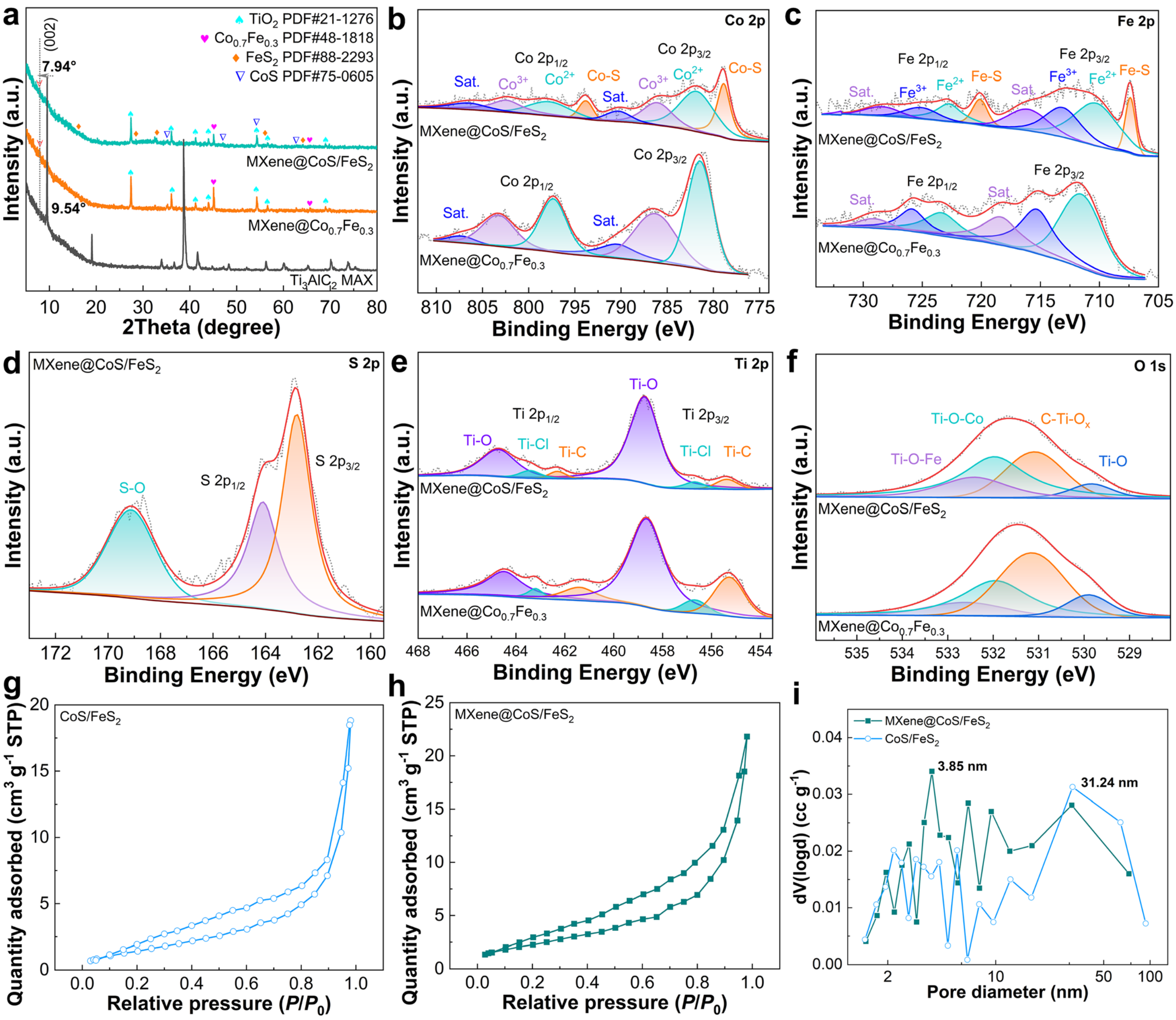

Fig. 4 (a) XRD patterns of the samples. High-resolution XPS spectra of (b) Co 2p, (c) Fe 2p, (d) S 2p, (e) Ti 2p, and (f) O 1s for MXene@$Co_{0.7}Fe_{0.3}$ and MXene@CoS/FeS_2. (g, h) N_2 adsorption–desorption isotherms and (i) pore size distribution plot of CoS/FeS_2 and MXene@CoS/FeS_2.

Co^{2+} and Fe^{2+} are effectively reduced by Al and form the $Co_{0.7}Fe_{0.3}$ alloy during the molten salt etching process. After undergoing sulfidation, MXene@CoS/FeS_2 demonstrates distinct peaks at 35.22°, 47.04°, 54.21°, and 62.62° that can be attributed to jaipurite CoS (PDF#75-0605), while peaks at 16.36°, 28.45°, 32.94°, 56.21°, and 64.21° are associated with pyrite FeS_2 (PDF#88-2293), proving the successful *in situ* transformation of $Co_{0.7}Fe_{0.3}$ to CoS/FeS_2 on the MXene. Compared to MXene@$Co_{0.7}Fe_{0.3}$, the (002) peak of MXene@CoS/FeS_2 exhibits a shift from 7.94° to 7.82°, indicating a slight expansion of the interlayer spacing. The XRD patterns of the control samples are also acquired (Fig. S20 and S21†). MAX@NaCl/KCl and MAX@NaCl/KCl–S display similar peaks to the original MAX (Fig. S20†), which indicates that the molten salt etching process using NaCl and KCl and the sulfidation process cannot significantly change the MAX phase. MXene@CoS shows peaks correspond to rutile TiO_2 and jaipurite CoS, while MXene@FeS_2 exhibits peaks which are attributed to rutile TiO_2 and pyrite FeS_2, indicating the successful deposition of CoS or FeS_2 on the MXene (Fig. S21†). Additionally, there are no peaks corresponding to TiO_2 in the MAX@NaCl/KCl and MAX@NaCl/KCl–S, indicating that the TiO_2 in MXene@CoS, MXene@FeS_2, and MXene@CoS/FeS_2 is the result of the reaction between Ti and H_2O (from $CoCl_2 \cdot 6H_2O$ or $FeCl_2 \cdot 4H_2O$).

The chemical composition and electronic states of elements in the samples were analyzed using X-ray photoelectron spectroscopy (XPS). The XPS survey spectra of MXene@$Co_{0.7}Fe_{0.3}$ and MXene@CoS/FeS_2 both exhibit characteristic peaks corresponding to Co 2p, Fe 2p, Ti 2p, C 1s, and O 1s, with an additional S 2p peak in MXene@CoS/FeS_2 (Fig. S22†). The high-resolution Co 2p XPS spectrum of MXene@CoS/FeS_2 can be deconvoluted into eight peaks (Fig. 4b), which can be assigned to Co^{2+} (797.4 eV, 781.0 eV), Co^{3+} (802.6 eV, 783.5 eV), Co–S bond (793.8 eV, 778.9 eV), and satellite peaks (806.3 eV, 787.5 eV).[39–41]

The binding energy of Co^{3+} in MXene@CoS/FeS_2 exhibits a positive shift compared to that in MXene@$Co_{0.7}Fe_{0.3}$, which can be attributed to the transfer of D-band electrons from Co to Fe species, thereby enhancing the electron-donating characteristics of MXene@CoS/FeS_2.[42,43] The high-resolution Fe 2p XPS spectrum of MXene@CoS/FeS_2 is deconvoluted into eight peaks that represent Fe^{2+} (722.7 eV, 710.3 eV), Fe^{3+} (725.1 eV, 713.1 eV), Fe–S bond (720.1 eV, 707.4 eV), and satellite peaks (728.4 eV, 716.0 eV) (Fig. 4c).[39,44,45] The peaks of Fe^{2+} and Fe^{3+} in MXene@CoS/FeS_2 exhibit a negative shift compared to those in MXene@$Co_{0.7}Fe_{0.3}$, along with the previously mentioned positive shift of Co^{3+}, demonstrating the interfacial electronic interaction between Co and Fe species, which can induce charge redistribution and boost the charge transfer within the catalyst.[46–48] During the sulfurization process, the introduction of sulfur atoms induces the formation of CoS and FeS_2 heterojunction interfaces, thereby facilitating electron transfer.[45,48,49] The high-resolution S 2p XPS spectrum of MXene@CoS/FeS_2 displays peaks at 162.3 eV, 163.6 eV, and 168.5 eV (Fig. 4d), corresponding to S $2p_{3/2}$, S $2p_{1/2}$, and a S–O bond, respectively, which validates the successful transformation of $Co_{0.7}Fe_{0.3}$ to CoS/FeS_2 *via* the sulfidation process.[39,50] The high-resolution Ti 2p XPS spectrum of MXene@CoS/FeS_2 can be fitted into a Ti–C bond (458.8 eV, 464.7 eV), Ti–Cl bond (456.9 eV, 463.4 eV), and Ti–O bond (455.4 eV, 462.2 eV) (Fig. 4e).[51,52] The Ti–C bond corresponds to the typical TiC_6 structure of $Ti_3C_2T_x$ MXene, while the Ti–Cl and Ti–O bonds verify that the MXene is terminated with –Cl and –O surface groups.[53] The Ti–C bond in the high-resolution C 1s XPS spectrum (Fig. S23†) and the Ti–O bond in the high-resolution O 1s XPS spectrum (Fig. 4f) of the MXene@CoS/FeS_2 further prove the above statement for the Ti 2p spectrum. Additionally, the presence of Ti–O–Co and Ti–O–Fe peaks in the O 1s spectrum validates that the $Co_{0.7}Fe_{0.3}$ nanopetal and CoS/FeS_2 heterojunction nanosheets are immobilized on the MXene through chemical bonding. XPS analysis was performed to detect the elemental composition of the MXene@CoS/FeS_2 heterostructure (Table S1†). It was found that the atomic ratios of each element deviated from the atomic ratios of the added metal salts. Therefore, further analysis was conducted using inductively coupled plasma optical emission spectroscopy (ICP-OES) to determine the content of metal elements in MXene@CoS/FeS_2 (Table S2†). The results showed that the content of Co and Fe is 19.61 wt% and 6.32 wt%, respectively, with a molar ratio of 2.94 : 1, which was close to the original feed ratio.

Furthermore, N_2 adsorption–desorption isotherms revealed the surface area and porous structure of the MXene@CoS/FeS_2 heterostructure. As shown in Fig. 4g and h, both CoS/FeS_2 and MXene@CoS/FeS_2 samples exhibit typical type IV isotherms with prominent H3-type hysteresis loops. This can be attributed to the lamellar structure of MXene@CoS/FeS_2, consistent with the results from SEM and TEM imaging. The Brunauer–Emmett–Teller (BET) surface area of MXene@CoS/FeS_2 (8.42 m^{-2} g^{-1}) is higher than that of the CoS/FeS_2 catalyst (5.64 m^{-2} g^{-1}), suggesting that the MXene can effectively inhibit the aggregation of CoS/FeS_2, leading to better exposure of active sites. The pore size distribution curve in Fig. 4i indicates that MXene@CoS/FeS_2 possesses abundant mesoporous (2–50 nm) structures. The mesoporous nanosheet structure and larger surface area of MXene@CoS/FeS_2 facilitate the full exposure of catalytic active sites and substance transfer, thereby accelerating the OER process.

Overall, the dual molten salt etching and *in situ* sulfidation processes have successfully anchored the CoS/FeS_2 heterojunction nanosheets on the MXene. SEM images show that CoS/FeS_2 heterostructure nanosheets are immobilized on the MXene, effectively preventing the aggregation of CoS/FeS_2 nanosheets and thereby enhancing the accessibility of active sites to the electrolyte. HRTEM images reveal the presence of CoS/FeS_2 heterojunctions in the MXene@CoS/FeS_2, which would function synergistically to reduce electron transfer resistance, shorten the electron transfer distance, and enhance the catalytic activity. Results of BET validate the high surface area and abundant mesopores of MXene@CoS/FeS_2, which facilitate the exposure of a large number of active sites and enhance mass transfer. XPS spectra prove the robust coupling between the CoS/FeS_2 heterojunctions and MXene through Ti–O–Co and Ti–O–Fe bonds, which facilitates efficient charge transfer and the overall structural stability of the catalyst. The intricate nanostructure of MXene@CoS/FeS_2 renders it a promising candidate in the field of OER.

To this end, the OER performance of MXene@CoS/FeS_2 catalysts was investigated using a three-electrode system. Firstly, a material optimization experiment was conducted prior to the systematic investigation of the catalyst's electrochemical performance. From the linear sweep voltammetry (LSV) curves, it can be seen that the synthesized MXene@CoS/FeS_2 demonstrates a reduced overpotential of 278 mV at 10 mA cm^{-2} with the addition of 0.2 g MAX, as compared to the addition of 0.1 and 0.3 g of MAX (Fig. S24a†). The inadequate addition of MAX may lead to an excessive deposition of transition metals on the MXene substrate, resulting in the formation of thick and uneven metal layers that can negatively impact the structural integrity and properties of the MXene@CoS/FeS_2. Meanwhile, the excessive amount of MAX can result in incomplete etching of the MAX and limited metal deposition on the MXene, which further leads to insufficient active sites and degradation of OER performance of the MXene@CoS/FeS_2. The OER activity increases initially and then decreases with the increase of the Co/Fe mole ratio, reaching optimal electrochemical performance at a Co/Fe mole ratio of 3 : 1 (Fig. S24b†). It can be observed that the MXene@CoS demonstrates superior OER activity compared to the MXene@FeS_2, possibly due to the unique electronic structure and catalytic properties of CoS. The Co–S bond in CoS is more polarized than the Fe–S bond in FeS_2, leading to a higher oxidation state of Co and enhanced catalytic activity. Additionally, the electrical conductivity of CoS is higher than that of FeS_2, enabling more efficient charge transfer.[54] These factors contribute to the superior OER performance of MXene@CoS compared to MXene@FeS_2.[55] Therefore, the overall OER activity tends to increase to some extent as the Co content increases. However, as the Co content continues to increase, there is a decrease in available Fe for coupling with Co and forming the heterostructure, thereby diminishing the synergistic effect and resulting in lower catalytic activity for the OER. Taking into account the combined influence of the aforementioned factors, the MXene@CoS/FeS_2 synthesized with a Co/Fe mole ratio of 3 : 1 exhibits the best OER performance. The MXene@CoS/FeS_2 synthesized at a sulfidation temperature of 350 °C displays superior OER activity compared to the samples obtained at 300 °C and 450 °C (Fig. S24c†). The insufficient sulfidation degree at low temperatures leads to a limited number of active sites on the surface of the catalyst, resulting in diminished OER performance. Meanwhile, an excessively high sulfidation temperature may induce phase transition and surface reconstruction in the CoS/FeS_2 heterostructure, consequently leading to a decline in the catalytic performance. The overpotentials under each set of experimental conditions are summarized and visually represented in a bar chart (Fig. S24d†). It can be seen that the optimized MXene@CoS/FeS_2 for the OER is synthesized under the following conditions: MAX amount of 0.2 g, Co/Fe mole ratio of 3 : 1, and sulfurization temperature of 350 °C. Throughout the subsequent text, the term "MXene@CoS/FeS_2" specifically denotes the optimized sample unless otherwise specified.

The electrochemical performance is then systematically evaluated to verify the advantages of the delicate nanostructure of MXene@CoS/FeS_2. The LSV curves demonstrate that the MXene@CoS/FeS_2 only requires an overpotential of 278 mV to achieve the current density of 10 mA cm^{-2}, better than those of

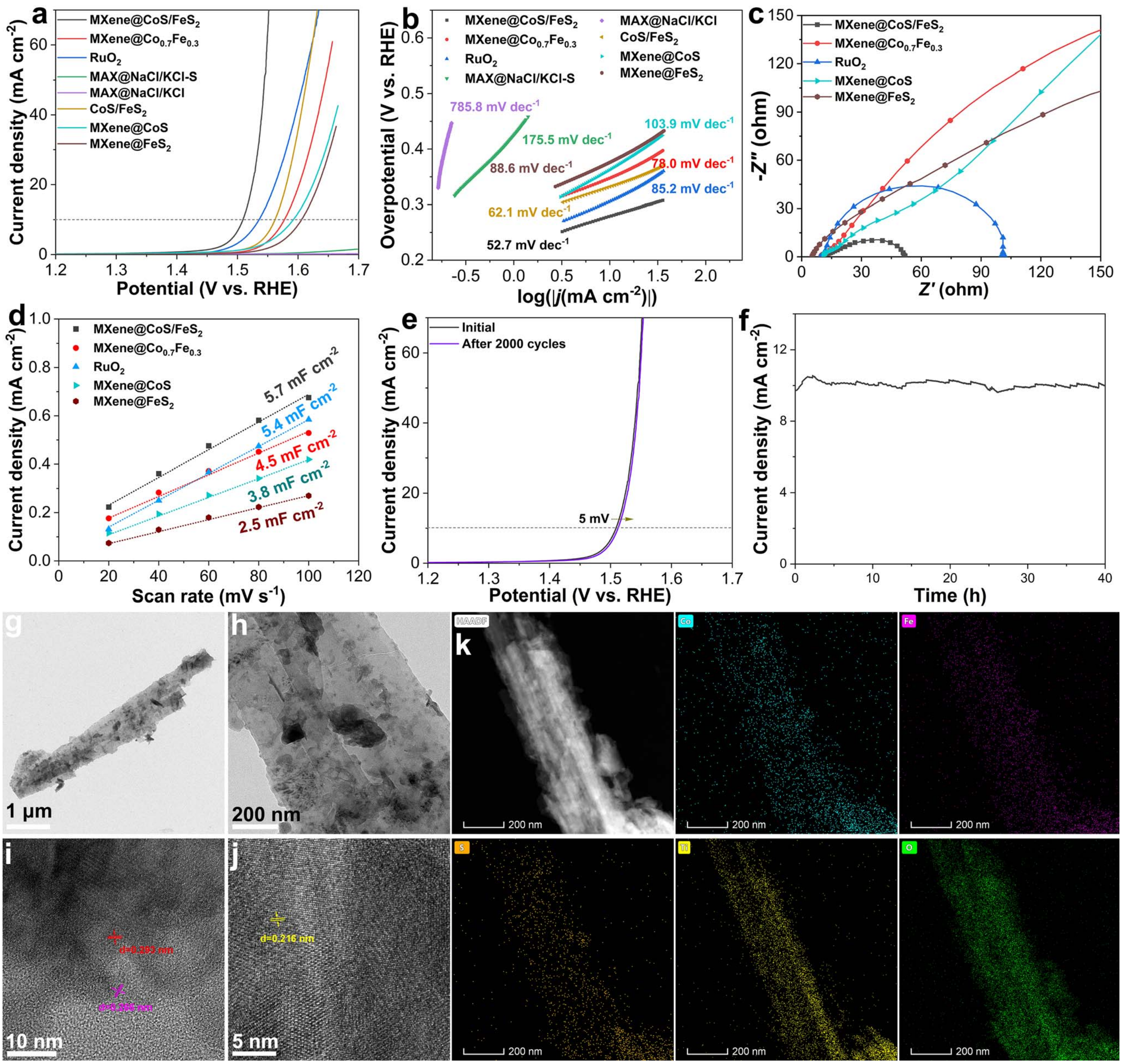

Fig. 5 (a) LSV polarization curves, (b) Tafel slopes, (c) Nyquist plots, and (d) C_{dl} curves of the catalysts. (e) LSV curves of MXene@CoS/FeS_2 before and after 2000 CV cycles. (f) Chronoamperometric curve of MXene@CoS/FeS_2. (g, h) TEM, (i, j) HRTEM, and (k) EDS elemental mapping images of MXene@CoS/FeS_2 after the long-term stability test.

RuO_2 (306 mV), MAX@NaCl/KCl (none), MAX@NaCl/KCl–S (none), MXene@$Co_{0.7}Fe_{0.3}$ (347 mV), CoS/FeS_2 (332 mV), MXene@CoS (363 mV), MXene@FeS_2 (375 mV) (Fig. 5a), and many previously reported OER catalysts (Table S3†). MAX@NaCl/KCl and MAX@NaCl/KCl–S demonstrate negligible OER performance due to the lack of discernible OER activity in the MAX phase. Compared with MXene@$Co_{0.7}Fe_{0.3}$, the overpotential of MXene@CoS/FeS_2 at 10 mA cm^{-2} is reduced by 69 mV, which might be ascribed to the enriched active sites and enhanced electronic structure (sulfur atoms modify the electronic structure of the metal centers) after the sulfidation. The electronic coupling between the metal and sulfur atoms also boosts the charge transfer processes involved in the OER. The overpotential of MXene@CoS/FeS_2 at 10 mA cm^{-2} is reduced by 54 mV compared to that of CoS/FeS_2, which can be attributed to the electrically conductive MXene substrate with a high specific surface area. Furthermore, compared with samples without MXene as a carrier, catalysts supported by MXene exhibit higher OER activity (Fig. S25†). The high specific surface area of MXene provides a vast space for the growth of CoS/FeS_2 nanosheets, thereby enhancing the accessibility of the electrolyte to catalytic sites. Moreover, the excellent conductivity facilitates electron transfer, further improving catalytic activity. The overpotential of MXene@CoS/FeS_2 at 10 mA cm^{-2} exhibits a reduction of 85 mV and 97 mV in comparison to those of MXene@CoS and MXene@FeS_2, respectively. The enhanced performance can be attributed to the formation of CoS/FeS_2 heterojunctions, which not only create abundant interfaces but also optimize the band structure and electronic properties in comparison to pure CoS and FeS_2. CoS/FeS_2 heterojunction nanosheets anchored on the electrically conductive MXene provide additional active sites, facilitate charge transfer, and promote the reaction kinetics, ultimately realizing the synergistic effect and improved catalytic activity. The Tafel slopes of the samples were further determined from the LSV curves to assess the electrochemical kinetics of the OER. The Tafel slope of MXene@CoS/FeS_2 is 52.72 mV dec^{-1}, lower than those of RuO_2 (85.17 mV dec^{-1}), MAX@NaCl/KCl (795.80 mV dec^{-1}), MAX@NaCl/KCl–S (175.51 mV dec^{-1}), MXene@$Co_{0.7}Fe_{0.3}$ (77.95 mV dec^{-1}), CoS/FeS_2 (62.11 mV dec^{-1}), MXene@CoS (103.86 mV dec^{-1}), and MXene@FeS_2 (110.79 mV dec^{-1}) (Fig. 5b). MXene@CoS/FeS_2 exhibits the fastest OER kinetics among all samples, as evidenced by its smallest Tafel slope. This might be ascribed to several reasons: (1) CoS/FeS_2 heterojunction nanosheets on MXene expose a larger number of active sites, facilitating mass transfer between the nanosheets and the electrolyte; (2) the synergistic effect between the electronically interacting CoS and FeS_2 enhances the catalytic activity; (3) the electrically conductive substrate of MXene facilitates efficient charge transfer between the CoS/FeS_2 heterojunction nanosheets and the electrode; (4) the robust interfacial contact between CoS/FeS_2 heterojunction nanosheets and MXene promotes efficient electron transfer at the interface.

Electrochemical impedance spectroscopy (EIS) can provide further insights into the catalytic kinetics. Results show that MXene@CoS/FeS_2 exhibits a small charge transfer resistance ($R_{ct} = 36.09\ \Omega$), which is lower than those of RuO_2 (91.81 Ω), MXene@$Co_{0.7}Fe_{0.3}$ (798.8 Ω), CoS/FeS_2 (263.3 Ω), MXene@CoS (176.7 Ω), and MXene@FeS_2 (453.9 Ω) (Fig. 5c). The efficient charge transfer and reduced charge transfer resistance of MXene@CoS/FeS_2 arise from various factors, including the large surface area of CoS/FeS_2 heterojunction nanosheets, the synergistic effect between CoS and FeS_2, the excellent electrical conductivity of MXene (Fig. S26†), and the interfacial electronic coupling between CoS/FeS_2 and MXene.

The electrochemical double-layer capacitance (C_{dl}) of these catalysts is determined by measuring cyclic voltammetry (CV) curves in the non-faradaic region (0.9–1.0 V *vs.* RHE) at different scan rates (Fig. S27†). The C_{dl} value of MXene@CoS/FeS_2 is calculated to be 5.7 mF cm^{-2}, surpassing those of RuO_2 (5.4 mF cm^{-2}), MXene@$Co_{0.7}Fe_{0.3}$ (4.5 mF cm^{-2}), MXene@CoS (3.8 mF cm^{-2}), and MXene@FeS_2 (2.5 mF cm^{-2}) (Fig. 5d). This indicates that the high specific surface area of MXene@CoS/FeS_2 provides more active sites for charge separation and ion adsorption at the electrode–electrolyte interface, promoting the formation of a double layer of charges with enhanced capacitance. Table S4† summarizes the C_{dl} and electrochemical surface area (ECSA) values of the samples, revealing that MXene@CoS/FeS_2 can provide more exposed active sites and exhibit higher intrinsic activity. ECSA-normalized LSV curves are shown in Fig. S28,† indicating that MXene@CoS/FeS_2 still exhibits the best catalytic activity.[56]

The electrochemical stability of MXene@CoS/FeS_2 is evaluated through consecutive CV scans and chronoamperometry (*i*–*t*) tests.[57] The results demonstrate that the overpotential of MXene@CoS/FeS_2 only increases by 5 mV even after undergoing 2000 CV cycles (Fig. 5e). The chronoamperometry test displays a slight decrease in current density even after 40 h of continuous operation at an overpotential of 280 mV for the MXene@CoS/FeS_2 electrode (Fig. 5f). The exceptional electrochemical stability of the MXene@CoS/FeS_2 can be attributed to the strong coupling between the CoS/FeS_2 heterojunction and MXene *via* Ti–O–Co and Ti–O–Fe bonds which promotes efficient charge transfer as well as the overall structural stability of the catalyst. Additionally, MXene serves as a support material that can prevent the aggregation of CoS/FeS_2 heterojunction nanosheets, ensuring better accessibility of the active sites to the electrolyte and maintaining stable catalytic performance over time.

TEM was further employed to observe the morphology of MXene@CoS/FeS_2 after stability testing in KOH solution. As shown in Fig. 5g and h, after durability testing in 1 M KOH, the morphology of MXene@CoS/FeS_2 remained relatively unchanged compared to its initial morphology. It is worth noting that after stability testing, lattice spacings of 0.293 nm corresponding to the (100) plane of CoS and 0.266 nm corresponding to the (200) plane of FeS_2 can be clearly observed in HRTEM images (Fig. 5i). In addition, by examining the HRTEM image of the MXene substrate region, a lattice spacing of 0.216 nm corresponding to the (105) crystal plane of MXene can be observed (Fig. 5j). Additionally, the EDS elemental mapping image of MXene@CoS/FeS_2 after stability testing for 40 h shows a uniform distribution of elements such as Co, Fe, S, Ti, C, and O (Fig. 5k). These results indicate that MXene@CoS/FeS_2

exhibits excellent stability. Additionally, XPS analysis was performed to investigate the chemical composition of MXene@CoS/FeS_2 after a long-term stability test (Fig. S29†). Compared with the catalysts before OER testing, the high-resolution XPS spectra of elements in the MXene@CoS/FeS_2 show similar valence states, further indicating the excellent stability of the MXene@CoS/FeS_2 catalyst. The Fe^{2+} and Fe^{3+} peaks, as well as the Co^{2+} and Co^{3+} peaks, show slight positive shifts, indicating the metal sulfides are slightly oxidized after OER testing. This is because metal sulfides are partially oxidized to the corresponding metal oxides/hydroxides under the oxidation potential of the OER, which serve as the active species for the OER.[56]

Overall, the delicate nanostructure of MXene@CoS/FeS_2 enables it to exhibit better OER performance than its MXene@$Co_{0.7}Fe_{0.3}$, CoS/FeS_2, MXene@CoS, and MXene@FeS_2 counterparts. This is attributed to the clever regulation achieved through the dual strategy of double-salt etching and *in situ* sulfurization. In this process, the CoS/FeS_2 heterojunction nanosheets and the MXene conductive substrate form strongly coupled Ti–O–Co and Ti–O–Fe bonds, significantly improving the efficiency of charge transfer. Sulfurization not only alters the metal electronic structure of MXene@$Co_{0.7}Fe_{0.3}$ but also enhances the charge transfer kinetics. Furthermore, employing the double-salt etching strategy, CoS/FeS_2 forms nanosheets with strong electronic interactions, simultaneously creating a heterojunction at the nanoscale, providing abundant active sites for catalytic reactions.

Density functional theory (DFT) calculations were further conducted to unveil the OER catalytic mechanism. Based on the XRD and HRTEM analysis, DFT calculations for MXene@CoS/FeS_2, MXene@CoS, and MXene@FeS_2 were carried out, and their optimized atomic structure models are presented in Fig. 6a–c. Considering the four basic proton–electron transfer steps in an alkaline medium, the adsorption models of the catalyst sequentially coupling with different oxygen-containing intermediates are illustrated in Fig. S30–S32.†[7,58] According to the Gibbs free energy calculations for these oxygen-containing intermediates (Fig. 6d), the rate-determining step (RDS) of MXene@CoS/FeS_2, MXene@CoS, and MXene@FeS_2 is found to be the step of *O to *OOH. At $U = 0$ V, the highest energy barrier for MXene@CoS/FeS_2 is 1.48 eV, significantly lower than those for MXene@CoS ($\Delta G = 2.68$ eV) and MXene@FeS2 ($\Delta G = 2.84$ eV). Furthermore, at $U = 1.23$ V, the RDSs of the three are similar, and the RDS energy barrier of MXene@CoS/FeS_2 is reduced to 0.25 eV (Fig. S33†). These results indicate that the formation of a heterointerface between CoS and FeS_2 optimizes the electronic structure of MXene@CoS/FeS_2, thereby lowering the RDS energy barrier.[59] These computational findings are consistent with the aforementioned OER performance, further indicating that the formation of the heterostructure is beneficial for OER performance.

By further analyzing the total density of states (TDOS) and the projected density of states (PDOS), we delve into the changes in electronic characteristics. As illustrated in Fig. 6e, it is

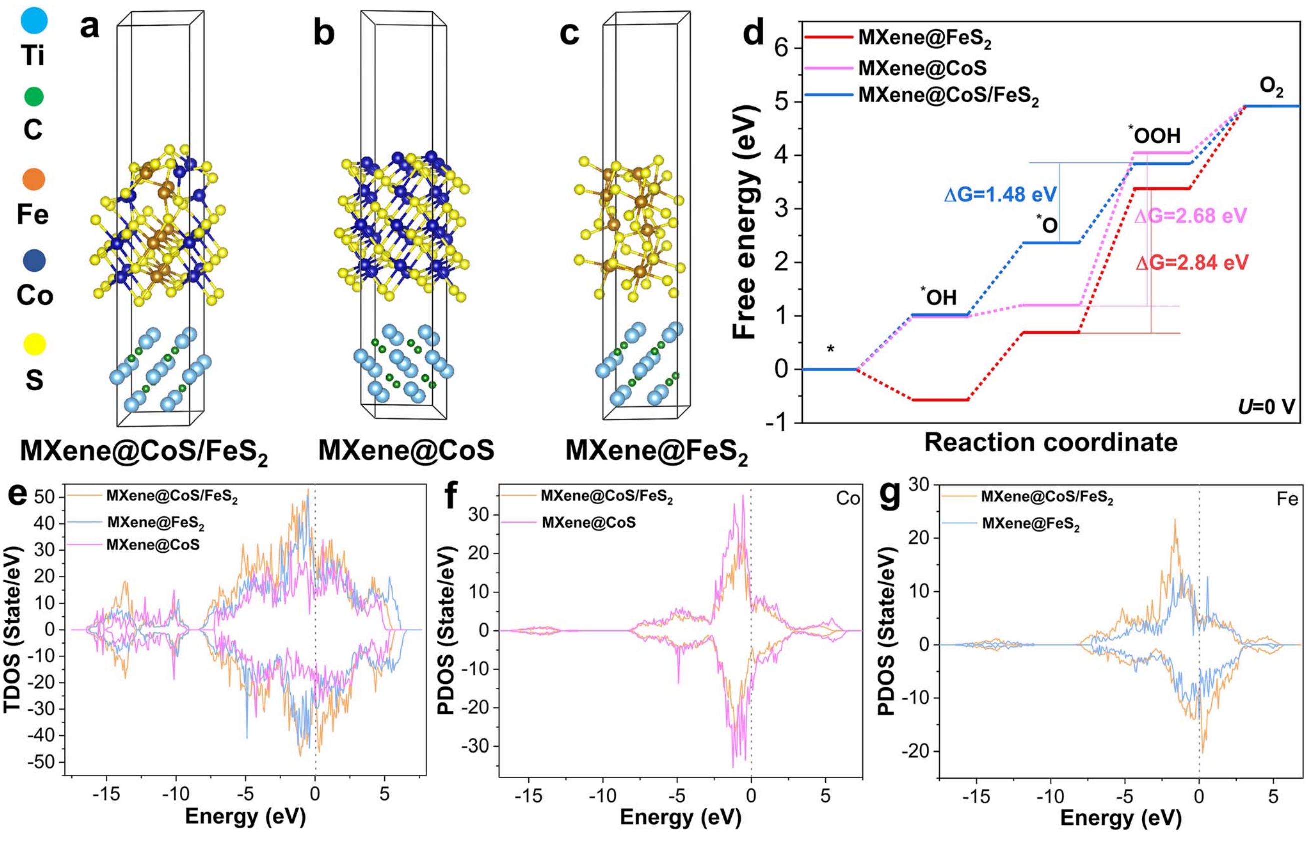

Fig. 6 Schematic models of the optimized (a) MXene@CoS/FeS_2, (b) MXene@CoS, and (c) MXene@FeS_2. (d) Calculated OER free-energy diagrams of the catalysts at a potential of 0 V. (e) TDOS curves of the samples. (f, g) PDOS curves of the catalysts.

observed that their overall density of states is greater than 0 near the Fermi level, indicating that these catalysts exhibit metallic characteristics.[60] Moreover, near the Fermi level, the TDOS of MXene@CoS/FeS_2 exceeds those of MXene@CoS and MXene@FeS_2, indicating that the formation of the CoS/FeS_2 heterostructure enhances the number of effective electron transfers. This implies superior electrical conductivity for the material, aligning with EIS test results.[59] Fig. 6f, g and S34† display the PDOS spectra of Co, Fe, and S elements, respectively. The PDOS of MXene@CoS near the Fermi level is higher than that of MXene@CoS/FeS_2, whereas the PDOS of MXene@FeS_2 is lower than that of MXene@CoS/FeS_2. This indicates that the formation of the CoS/FeS_2 heterostructure leads to a rearrangement of electron density at the interface, where electrons transfer from Co to Fe atoms, thereby increasing the electron density around Fe atoms. This is consistent with the XPS test results. These findings further indicate a strong electronic interaction between CoS and FeS_2. The construction of the CoS/FeS_2 heterostructure accelerates spontaneous electron transfer and enriches active sites, which is highly beneficial for the adsorption and desorption of OER intermediates. This is the key reason why MXene@CoS/FeS_2 exhibits superior OER activity.

4. Conclusions

This work has employed a dual molten salt etching strategy and subsequent sulfidation to immobilize CoS/FeS_2 heterojunction nanosheets onto an electrically conductive MXene (MXene@CoS/FeS_2) for efficient OER. The straightforward and efficient preparation process eliminates the need for HF, thereby facilitating the production of MXene@CoS/FeS_2 on a large scale while ensuring both safety and environmental friendliness. Experimental results have proved the large specific surface area of MXene@CoS/FeS_2, the strong electronic interaction between CoS and FeS_2, and the interfacial electronic coupling between the MXene and CoS/FeS_2 heterojunction nanosheets *via* Ti–O–Co and Ti–O–Fe bonds, which expose more electrocatalytic active sites, boost the electron transfer kinetics, and ensure the structural stability for the OER. Consequently, the MXene@CoS/FeS_2 exhibits a low overpotential (278 mV achieved at 10 mA cm^{-2}) and outstanding stability (over 40 h). DFT calculations indicate that the electron transfer at the CoS/FeS_2 interface effectively reduces the energy barrier of the RDS for MXene@CoS/FeS_2. The transition metal sulfide heterojunction has been successfully anchored on the MXene *via* a simple and eco-friendly method, which may provide some valuable insight into improving the electrocatalytic activity of catalysts by integrating MXenes with multi-transition metal chalcogenides, phosphides, *etc.*, for efficient OER.

Author contributions

Zuliang Zhang: data curation, investigation, methodology, writing – original draft, writing – review & editing. Tian Liang: methodology, software, writing – review & editing. Chulong Jin: investigation, writing – review & editing. Shuyi Zhang: data curation, software, writing – review & editing. Yuanyuan Cui: software, writing – review & editing. Jinxing Chen: conceptualization, resources, writing – review & editing. Xiaojun Zeng: conceptualization, funding acquisition, project administration, resources, supervision, writing – original draft, writing – review & editing.

Conflicts of interest

The authors declare that they have no conflict of interest.

Acknowledgements

This work was supported by the National Natural Science Foundation of China (No. 22269010), the Jiangxi Provincial Natural Science Foundation (No. 20224BAB214021), the Major Research Program of Jingdezhen Ceramic Industry (No. 2023ZDGG002), the Opening Project of National Engineering Research Center for Domestic & Building Ceramics (No. GXZX2302), and the Scientific Research Foundation of Hubei University of Science and Technology (BK202314, 2022ZX10).

References

1 X. J. Zeng, Q. Q. Zhang, C. L. Jin, H. Huang and Y. F. Gao, Fe-induced electronic transfer and structural evolution of lotus pod-like CoNiFeP_x@P, N-C heterostructure for sustainable oxygen evolution, *Energy Environ. Mater.*, 2023, e12628.

2 X. J. Zeng, Y. Y. Ye, Y. Q. Wang, R. Yu and M. Moskovits, Honeycomb-like MXene/NiFeP_x-NC with "continuous"single-crystal enabling high activity and robust durability in electrocatalytic oxygen evolution reactions, *J. Adv. Ceram.*, 2023, **12**(3), 553–564.

3 J. P. Sun, Z. Zhao, J. Li, Z. Z. Li and X. C. Meng, Recent advances in electrocatalytic seawater splitting, *Rare Met.*, 2023, **42**(3), 751–768.

4 P. Y. Kuang, Z. R. Ni, B. C. Zhu, Y. Lin and J. G. Yu, Modulating the d-Band Center Enables Ultrafine Pt_3Fe Alloy Nanoparticles for Ph-Universal Hydrogen Evolution Reaction, *Adv. Mater.*, 2023, **35**(41), 2303030.

5 Y. P. Zuo, N. Antonatos, L. Děkanovský, J. Luxa, J. D. Elliott, D. Gianolio, F. Guzzetta, S. Mourdikoudis, J. Regner, R. Málek and Z. Sofer, Defect Engineering in Two-Dimensional Layered $PdTe_2$ for Enhanced Hydrogen Evolution Reaction, *ACS Catal.*, 2023, **13**(4), 2601–2609.

6 H. Q. Zhang, X. J. Zeng, Q. Q. Zhang, Z. L. Zhang, C. L. Jin and R. H. Yu, Dual template-induced construction of three-dimensional porous SiO_2/NC/Co-CNTs heterostructure with highly dispersed active sites for efficient oxygen evolution reaction, *Tungsten*, 2023, DOI: 10.1007/s42864-023-00253-x.

7 X. J. Zeng, H. Q. Zhang, R. H. Yu, G. D. Stucky and J. S. Qiu, A phase and interface co-engineered MoP_xS_y@$NiFeP_xS_y$@NPS-C hierarchical heterostructure for sustainable oxygen evolution reaction, *J. Mater. Chem. A*, 2023, **11**(26), 14272–14283.

8 X. J. Zeng, D. R. Duan, X. F. Zhang, X. H. Li, K. Li, R. H. Yu and M. Moskovits, Doping and interface engineering in a sandwich $Ti_3C_2T_x/MoS_{2-x}P_x$ heterostructure for efficient hydrogen evolution, *J. Mater. Chem. C*, 2022, **10**(11), 4140–4147.

9 C. D. Kou, J. R. Han, H. B. Wang, M. Han and H. Y. Liang, Unveiling the role of Zn dopants in NiFe phosphide nanosheet for oxygen evolution reaction, *Prog. Nat. Sci.: Mater. Int.*, 2023, **33**(1), 74–82.

10 T. J. Wang, Y. C. Jiang, J. W. He, F. M. Li, Y. Ding, P. Chen and Y. Chen, Porous palladium phosphide nanotubes for formic acid electrooxidation, *Carbon Energy*, 2022, **4**(3), 283–293.

11 M. Wang, L. Zhang, Y. J. He and H. G. Zhu, Recent advances in transition-metal-sulfide-based bifunctional electrocatalysts for overall water splitting, *J. Mater. Chem. A*, 2021, **9**(9), 5320–5363.

12 Y. N. Guo, T. Park, J. W. Yi, J. Henzie, J. Kim, Z. L. Wang, B. Jiang, Y. Bando, Y. Sugahara, J. Tang and Y. Yamauchi, Nanoarchitectonics for transition-metal-sulfide-based electrocatalysts for water splitting, *Adv. Mater.*, 2019, **31**(17), 1807134.

13 Y. N. Chen, S. M. Xu, S. Z. Zhu, R. J. Jacob, G. Pastel, Y. B. Wang, Y. J. Li, J. Q. Dai, F. J. Chen, H. Xie, B. Y. Liu, Y. G. Yao, L. G. Salamanca-Riba, M. R. Zachariah, T. Li and L. B. Hu, Millisecond synthesis of CoS nanoparticles for highly efficient overall water splitting, *Nano Res.*, 2019, **12**, 2259–2267.

14 S. C. Yan, K. Wang, F. Zhou, S. R. Lin, H. Z. Song, Y. Shi and J. Yao, Ultrafine Co: FeS_2/CoS_2 heterostructure nanowires for highly efficient hydrogen evolution reaction, *ACS Appl. Energy Mater.*, 2019, **3**(1), 514–520.

15 Y. X. Li, J. Yin, L. An, M. Lu, K. Sun, Y. Q. Zhao, D. Q. Gao, F. Y. Cheng and P. X. Xi, FeS_2/CoS_2 interface nanosheets as efficient bifunctional electrocatalyst for overall water splitting, *Small*, 2018, **14**(26), 1801070.

16 E. Vijayakumar, S. Ramakrishnan, C. Sathiskumar, D. J. Yoo, J. Balamurugan, H. S. Noh, D. Kwon, Y. H. Kim and H. G. Lee, MOF-derived CoP-nitrogen-doped carbon@NiFeP nanoflakes as an efficient and durable electrocatalyst with multiple catalytically active sites for OER, HER, ORR and rechargeable zinc-air batteries, *Chem. Eng. J.*, 2022, **428**, 131115.

17 D. Jena, K. Banerje and G. H. Xing, Intimate contacts, *Nat. Mater.*, 2014, **13**(12), 1076–1078.

18 J. Xu, G. L. Shao, X. Tang, F. Lv, H. Y. Xiang, C. F. Jing, S. Liu, S. Dai, Y. G. Li, J. Luo and Z. Zhou, Frenkel-defected monolayer MoS_2 catalysts for efficient hydrogen evolution, *Nat. Commun.*, 2022, **13**(1), 2193.

19 Y. Tang, C. H. Yang, X. T. Xu, Y. Q. Kang, J. Henzie, W. X. Que and Y. Yamauchi, MXene nanoarchitectonics: defect-engineered 2D MXenes towards enhanced electrochemical water splitting, *Adv. Energy Mater.*, 2022, **12**(12), 2103867.

20 C. E. Park, R. A. Senthil, G. H. Jeong and M. Y. Choi, Architecting the High-Entropy Oxides on 2D MXene Nanosheets by Rapid Microwave-Heating Strategy with Robust Photoelectrochemical Oxygen Evolution Performance, *Small*, 2023, 2207820.

21 X. J. Zeng, X. Jiang, Y. Ning, F. Y. Hu and B. B. Fan, Construction of dual heterogeneous interface between zigzag-like Mo-MXene nanofibers and small CoNi@NC nanoparticles for electromagnetic wave absorption, *J. Adv. Ceram.*, 2023, **12**(8), 1562–1576.

22 T. V. Nguyen, M. Tekalgne, T. P. Nguyen, Q. V. Le, S. H. Ahn and S. Y. Kim, Electrocatalysts based on MoS_2 and WS_2 for hydrogen evolution reaction: An overview, *Battery Energy*, 2023, **2**, 20220057.

23 X. J. Zeng, C. Zhao, Y. Yin, T. L. Nie, N. Xie, R. H. Yu and G. D. Stucky, Construction of $NiCo_2O_4$ nanosheets-covered $Ti_3C_2T_x$ MXene heterostructure for remarkable electromagnetic microwave absorption, *Carbon*, 2022, **193**, 26–34.

24 S. L. Han, Y. Chen, Y. N. Hao and Y. Y. Xie, Multi-dimensional hierarchical CoS_2@MXene as trifunctional electrocatalysts for zinc-air batteries and overall water splitting, *Sci. China Mater.*, 2021, **64**, 1127–1138.

25 Y. Y. Xie, H. Z. Yu, L. M. Deng, R. S. Amin, D. S. Yu, A. E. Fetohi, M. Y. Maximov, L. L. Li, K. M. El-Khatib and S. J. Peng, Anchoring stable FeS_2 nanoparticles on MXene nanosheets *via* interface engineering for efficient water splitting, *Inorg. Chem. Front.*, 2022, **9**(4), 662–669.

26 H. Y. Zou, B. He, P. Y. Kuang, J. G. Yu and K. Fan, Metal-organic framework-derived nickel-cobalt sulfide on ultrathin MXene nanosheets for electrocatalytic oxygen evolution, *ACS Appl. Mater. Interfaces*, 2018, **10**(26), 22311–22319.

27 M. P. Chen, D. Liu, B. Y. Zi, Y. Y. Chen, D. Liu, X. Y. Du, F. F. Li, P. F. Zhou, Y. Ke, J. L. Li, K. H. Lo, C. T. Kwok, W. F. Ip, S. Chen, S. P. Wang, Q. J. Liu and H. Pan, Remarkable synergistic effect in cobalt-iron nitride/alloy nanosheets for robust electrochemical water splitting, *J. Energy Chem.*, 2022, **65**, 405–414.

28 Q. Xu, L. Ding, Y. Y. Wen, W. J. Yang, H. J. Zhou, X. Z. Chen, J. Street, A. G. Zhou, W. J. Ong and N. Li, High photoluminescence quantum yield of 18.7% by using nitrogen-doped Ti_3C_2 MXene quantum dots, *J. Mater. Chem. C*, 2018, **6**, 6360–6369.

29 W. W. Xu, Q. L. Wu, J. Gwon and J. W. Choi, Ice-Crystal-Templated "Accordion-Like" Cellulose Nanofiber/MXene Composite Aerogels for Sensitive Wearable Pressure Sensors, *ACS Sustainable Chem. Eng.*, 2023, **11**(8), 3208–3218.

30 Z. M. Li, S. S. Xin, Y. R. Zhang, Z. F. Zhang, C. P. Li, C. J. Li, R. Bao, J. H. Yi, M. L. Xu and J. S. Wang, Boosting elementary steps kinetics towards energetic alkaline hydrogen evolution *via* dual sites on phase-separated Ni-Cu-Mn/hydroxide, *Chem. Eng. J.*, 2023, **451**, 138540.

31 W. Q. Li, H. Zhang, M. Z. Hong, L. L. Zhang, X. Feng, M. F. Shi, W. X. Hu and S. C. Mu, Defective RuO_2/TiO_2 nano-heterostructure advances hydrogen production by electrochemical water splitting, *Chem. Eng. J.*, 2022, **431**, 134072.

32 J. Wu, W. D. Zhong, C. F. Yang, W. L. Xu, R. Zhao, H. Xiang, Q. Zhang, X. K. Li and N. J. Yang, Sulfur-vacancy rich

nonstoichiometric TiS_{2-x}/NiS heterostructures for superior universal hydrogen evolution, *Appl. Catal., B*, 2022, **310**, 121332.

33 L. Y. Wu, P. P. Guo, X. Wang, H. Y. Li, X. R. Zhang, K. Y. Chen and P. Zhou, The synergy of sulfur vacancies and heterostructure on CoS@FeS nanosheets for boosting the peroxymonosulfate activation, *Chem. Eng. J.*, 2022, **446**, 136759.

34 X. J. Zeng, Y. N. Tan, L. Xia, Q. Q. Zhang and G. D Stucky, MXene-derived Ti_3C_2-Co-TiO_2 nanoparticle arrays *via* cation exchange for highly efficient and stable electrocatalytic oxygen evolution, *Chem. Commun.*, 2023, **59**(7), 880–883.

35 J. Li, M. Guo, X. Yang, J. L. Wang, K. X. Wang, A. R. Wang, F. C. Lei, P. Hao, J. F. Xie and B. Tang, Dual elemental modulation in cationic and anionic sites of the multi-metal Prussian blue analogue pre-catalysts for promoted oxygen evolution reaction, *Prog. Nat. Sci.: Mater. Int.*, 2022, **32**(6), 705–714.

36 B. Sarfraz, M. T. Mehran, M. M. Baig, S. R. Naqvi, A. Khoja and F. Shahzad, HF free greener Cl-terminated MXene as novel electrocatalyst for overall water splitting in alkaline media, *Int. J. Energy Res.*, 2022, **46**(8), 10942–10954.

37 X. J. Zeng, C. Zhao, T. L. Nie, Z. Y. Shen, R. H. Yu and G. D. Stucky, Construction of 0D/1D/2D MXene nanoribbons-NiCo@NC hierarchical network and their coupling effect on electromagnetic wave absorption, *Mater. Today Phys.*, 2022, **28**, 100888.

38 H. M. Ding, Y. B. Li, J. Lu, K. Luo, K. Chen, M. Li, P. O. Å. Persson, L. Hultman, P. Eklund, S. Y. Du, Z. G. Huang, Z. F. Chai, H. J. Wang, P. Huang and Q. Huang, Synthesis of MAX phases Nb_2CuC and $Ti_2(Al_{0.1}Cu_{0.9})$ N by A-site replacement reaction in molten salts, *Mater. Res. Lett.*, 2019, **7**(12), 510–516.

39 B. Wang, Y. F. Chen, X. Q. Wang, X. J. Zhang, Y. Hu, B. Yu, D. X. Yang and W. L. Zhang, A microwave-assisted bubble bursting strategy to grow Co_8FeS_8/CoS heterostructure on rearranged carbon nanotubes as efficient electrocatalyst for oxygen evolution reaction, *J. Power Sources*, 2020, **449**, 227561.

40 S. Shit, S. Chhetri, W. Jang, N. C. Murmu, H. Koo, P. Samanta and T. Kuila, Cobalt sulfide/nickel sulfide heterostructure directly grown on nickel foam: an efficient and durable electrocatalyst for overall water splitting application, *ACS Appl. Mater. Interfaces*, 2018, **10**(33), 27712–27722.

41 A. Mahsud, J. N. Chen, X. L. Yuan, F. L. Lyu, Q. X. Zhong, J. X. Chen, Y. D. Yin and Q. Zhang, Self-templated formation of cobalt-embedded hollow N-doped carbon spheres for efficient oxygen reduction, *Nano Res.*, 2021, **14**, 2819–2825.

42 X. J. Shi, B. B. He, L. Zhao, Y. S. Gong, R. Wang and H. W. Wang, FeS_2-CoS_2 incorporated into nitrogen-doped carbon nanofibers to boost oxygen electrocatalysis for durable rechargeable Zn-air batteries, *J. Power Sources*, 2021, **482**, 228955.

43 Y. S. Zhang, Y. L. Jia, M. Song, N. R. Xiao, C. Y. Dai, Y. Sun, L. L. Wang, Y. N. Zhao, J. G. Yu and Y. N. Qu, One-step construction of NiCo alloy particles encapsulated in N-doped carbon frameworks application for overall water splitting, *Colloids Surf., A*, 2023, **658**, 130665.

44 Z. J. Chen, R. J. Zheng, S. M. Deng, W. F. Wei, W. Wei, B. J. Ni and H. Chen, Modular design of an efficient heterostructured FeS_2/TiO_2 oxygen evolution electrocatalyst *via* sulfidation of natural ilmenites, *J. Mater. Chem. A*, 2021, **9**, 25032–25041.

45 X. Yu, J. Mei, Y. S. Du, X. H. Cheng, X. Wang and Q. Wu, Engineered interface of three-dimensional coralliform NiS/FeS_2 heterostructures for robust electrocatalytic water cleavage, *Nano Res.*, 2024, **17**, 4693–4701.

46 W. X. Xu, Y. Wei, S. B. Zhou, R. Sun, X. Huang, S. Han, S. Z. Wang and J. B. Jiang, Structural design strategy improving catalytic activity of binary metal sulfides interface for efficient water splitting electrocatalysts, *Electrochim. Acta*, 2023, **454**, 142377.

47 F. L. Gong, Y. H. Liu, Y. Zhao, W. Liu, G. Zeng, G. Q. Wang, Y. H. Zhang, L. H. Gong and J. Liu, Universal Sub-Nanoreactor Strategy for Synthesis of Yolk-Shell MoS_2 Supported Single Atom Electrocatalysts toward Robust Hydrogen Evolution Reaction, *Angew. Chem., Int. Ed.*, 2023, e202308091.

48 L. An, Y. X. Li, M. C. Luo, J. Yin, Y. Q. Zhao, C. L. Xu, F. Y. Cheng, Y. Yang, P. X. Xi and S. J. Guo, Atomic-level coupled interfaces and lattice distortion on CuS/NiS_2 nanocrystals boost oxygen catalysis for flexible Zn-air batteries, *Adv. Funct. Mater.*, 2017, **27**(42), 1703779.

49 Y. Q. Yang, K. Zhang, H. L. Lin, X. Li, H. C. Chan, L. H. Yang and Q. S. Gao, MoS_2-Ni_3S_2 heteronanorods as efficient and stable bifunctional electrocatalysts for overall water splitting, *ACS Catal.*, 2017, **7**(4), 2357–2366.

50 S. Zhang, S. R. Zhao, S. J. Huang, B. Hu, M. H. Wang, Z. H. Zhang, L. H. He and M. Du, Photocatalytic degradation of oxytetracycline under visible light by nanohybrids of CoFe alloy nanoparticles and nitrogen-/sulfur-codoped mesoporous carbon, *Chem. Eng. J.*, 2021, **420**, 130516.

51 J. N. Hu, C. Y. Liang, J. D. Li, C. W. Lin, Y. J. Liang, H. Wang, X. Li, Q. L. Wang and D. W. Dong, Tailoring the plasmonic properties of gold-liposome nanohybrids as a potential powerful tool for light-mediated therapies, *Carbon*, 2023, **204**, 136–146.

52 X. J. Zeng, C. Zhao, X. Jiang, R. H. Yu and R. C. Che, Functional Tailoring of Multi-Dimensional Pure MXene Nanostructures for Significantly Accelerated Electromagnetic Wave Absorption, *Small*, 2023, **19**, 2303393.

53 P. F. Huang, H. J. Ying, S. L. Zhang, Z. Zhang and W. Q. Han, Molten salts etching route driven universal construction of MXene/transition metal sulfides heterostructures with interfacial electronic coupling for superior sodium storage, *Adv. Energy Mater.*, 2022, **12**, 2202052.

54 L. Trotochaud, S. L. Young, J. K. Ranney and S. W. Boettcher, Nickel-iron oxyhydroxide oxygen-evolution electrocatalysts: the role of intentional and incidental iron incorporation, *J. Am. Chem. Soc.*, 2014, **136**(18), 6744–6753.

55 G. A. Gebreslase, M. V. Martínez-Huerta and M. J. Lázaro, Recent progress on bimetallic NiCo and CoFe based electrocatalysts for alkaline oxygen evolution reaction: A review, *J. Energy Chem.*, 2022, **67**, 101–137.

56 P. Mukherjee, K. Sathiyan, R. Bar-Ziv and T. Zidki, Chemically etched Prussian blue analog-WS_2 composite as a precatalyst for enhanced electrocatalytic water oxidation in alkaline media, *Inorg. Chem.*, 2023, **62**(35), 14484–14493.

57 M. Y. Chu, J. L. Huang, J. Gong, Y. Qu, G. L. Chen, H. Yang, X. C. Wang, Q. X. Zhong, C. W. Deng, M. H. Cao, J. X. Chen, X. L. Yuan and Q. Zhang, Synergistic combination of Pd nanosheets and porous $Bi(OH)_3$ boosts activity and durability for ethanol oxidation reaction, *Nano Res.*, 2022, **15**, 3920–3926.

58 J. Zhang, T. Wang, D. Pohl, B. Rellinghaus, R. Dong, S. H. Liu, X. D. Zhuang and X. L. Feng, Interface engineering of MoS_2/Ni_3S_2 heterostructures for highly enhanced electrochemical overall-water-splitting activity, *Angew. Chem., Int. Ed.*, 2016, **128**(23), 6814–6819.

59 F. Q. Li, H. Wu, S. C. Lv, Y. J. Ma, B. Wang, Y. L. Ren, C. Wang, Y. X. Shi, H. R. Jian, J. Gu, S. C. Tang and X. K. Meng, Two birds with one stone: contemporaneously enhancing OER catalytic activity and stability for dual-phase medium-entropy metal sulfides, *Small*, 2023, **20**(11), 2309025.

60 H. Wang, Y. Zhou and S. Tao, CoP-CoOOH heterojunction with modulating interfacial electronic structure: a robust biomass-upgrading electrocatalyst, *Appl. Catal., B*, 2022, **315**, 121588.